Second-sphere hydrogen-bonding enhances heterogeneous electrocatalytic CO 2 to CO reduction by iron porphyrins in water

Chanjuan Zhang, Diana Dragoe, François Brisset, Bernard Boitrel, Benedikt Lassalle-Kaiser, Winfried Leibl, Zakaria Halime, Ally Aukauloo

ARTICLE

Second-Sphere Hydrogen-Bonding Enhances Heterogenous Electrocatalytic CO_2 Reduction by Iron Porphyrin in water

Chanjuan Zhang,[a] Diana Dragoe,[a] François Brisset,[a] Bernard Boitrel,[b] Benedikt Lassalle-Kaiser,[d] Winfried Leibl,[c] Zakaria Halime*[a] and Ally Aukauloo*[a,c]

Received 00th January 20xx,
Accepted 00th January 20xx

DOI: 10.1039/x0xx00000x

Intense efforts are currently being injected in discovering cost-effective catalysts for the selective reduction of carbon dioxide (CO_2). Much advances have indeed been realized in the design of molecular complexes containing second coordination chemical functionalities that have contributed to boost the homogeneous electrocatalytic activity. Implementing these chemical facets in heterogeneous catalysis can give access to an improved catalysis while opening at the same time the way for practical and sustainable applications. Here we report the catalytic properties for CO_2 electroreduction of a heterogenized molecular iron-porphyrin catalyst bearing a bioinspired second coordination sphere (**UrFe**) in water as a green solvent and proton source. The immobilization of this catalyst on a multiwall carbon nanotubes (MWCNTs)/carbon paper (CP) modified electrode allows to overcome its hydrophobicity limitation and to take full advantage of the synergic effect observed in homogeneous catalysis between water molecules and the urea groups in the second sphere. The obtained modified electrode displays a better selectivity and stability and more than one order of magnitude higher effective turnover frequency (eTOF) than that of a similar modified electrode containing iron-porphyrin analogues without a second sphere. One of the highest eTOF values reported in the literature was reached when a -0.78 V *vs*. RHE potential was applied with over 90% selectivity for CO production for 2 hours.

1. Introduction

The electrochemical conversion of carbon dioxide (CO_2) and water into useful products, powered by renewable electricity, is a major challenge towards closing the carbon cycle.[1] Another alternative, is to develop integrated systems that can realize the capture of photons to engine the catalytic reactions.[2] However, CO_2 is a thermodynamically and kinetically very stable molecule and its electroreduction requires the use of a catalyst to decrease the overpotential and energy input needed to bind and transform this highly stable molecule.[3-5] In homogeneous catalysis, the tunability of the catalyst through ligand design and the possibility to access precious spectroscopic information on the reaction mechanism, have contributed to the identification of important parameters that impact catalyst performance. [3-5] Iron porphyrins are among the most active and selective catalysts for homogeneous CO_2 electroreduction to CO.[6, 7] Taking inspiration from the crucial role that the second coordination sphere plays in the reactivity of Carbon Monoxide DeHydrogenase (CODH) active site,[8-10] molecular chemists have implemented different functionalities in the second sphere of iron porphyrins[11-15] such as a local proton source, (i.e. phenols,[6, 16-18] carboxylic acids[19]), reaction intermediate stabilizers (ammonium cations,[20] imidazolium moieties[21, 22]) and H-bond donors (amides,[23, 24] guanidine,[16] and triazoles[23, 25]). These modifications have successfully led to a significant decrease in the overpotential while improving the catalytic turnover numbers (TONs) and frequencies (TOFs). At this juncture, chemists are heading to bring molecular catalysts on the surface of electrodes to develop hybrid systems for heterogeneous catalysis with the perspective to develop compartmental (photo)cathodes to couple with a (photo)anode for the complete solar to fuel production.[26-32] We have recently reported a biomimetic second coordination sphere inducing multipoint hydrogen-bonding patterns that can greatly boost CO_2 reduction by an iron-porphyrin catalyst (**UrFe**, see Figure 1a) in organic solvents such as dimethylformamide (DMF) (Figure 1a).[33] A detailed mechanistic study has shown that when a limited amount of water (under 16%) is added to DMF as a proton source, in addition to improving CO_2 capture by stabilizing Fe^{I}-CO_2^{-} intermediates, the urea groups in the second sphere also participate in establishing a water molecule network that supplies the protons needed for CO_2 reduction.[33, 34] However, increasing the water content above 16% has the reverse effect of inhibiting the catalytic activity. Here, we provide evidences that this reverse effect results from the precipitation of the catalyst due to its hydrophobic character.

[a] *Université Paris-Saclay, CNRS, Institut de chimie moléculaire et des matériaux d'Orsay, 91405, Orsay, France. E-mail: ally.aukauloo@universite-paris-saclay.fr, zakaria.halime@universite-paris-saclay.fr*
[b] *Institut des Sciences Chimiques de Rennes, UMR CNRS 6226, Université de Rennes 1, Rennes cedex, France*
[c] *Université Paris-Saclay, CEA, Institute for Integrative Biology of the Cell (I2BC), 91198, Gif-sur-Yvette, France.*
[d] *Synchrotron SOLEIL, l'Orme des Merisiers, Saint-Aubin, 91191 Gif-sur-Yvette, France.*

† Electronic Supplementary Information (ESI) available: Controlled potential electrolysis coupled to gas chromatograpy analysis, ATR-FTIR spectra and XANES spectra. See DOI: 10.1039/x0xx00000x

To overcome this limitation, the approach consisting of confining molecular catalysts at the surface of electrodes offers the opportunity to combining the better understanding/tunability of molecular systems with the practicality of heterogeneous systems. In this configuration, despite the hydrophobicity of the catalyst, the electrocatalytic reduction of CO_2 can be performed in water as a clean and sustainable solvent and a proton source. Molecular catalysts can be immobilized on the electrode surface by different means,[14, 35-38] including covalent grafting,[39-46] electro-polymerization,[47-50] physisorption and electrostatic interaction.[51-55] Among these methods, π-π physisorption on multiwall carbon nanotubes (MWCNTs) is of particular interest to immobilize aromatic molecules such as porphyrins for their high stability, electrical conductivity and high surface area.[28, 56-61] Here we report a clear example on how the findings from enhancing CO_2-to-CO electroreduction with bioinspired second sphere functions at the molecular level can be further at play in heterogenous catalysis. The modified electrode was prepared by depositing impregnated MWCNTs with **UrFe** catalyst on the surface of carbon paper. Such a hybrid device enables the export of the synergistic effect operating from the urea groups and water molecules in homogenous to heterogenous catalysis under environmentally acceptable conditions. In the light of a comparative study with a modified electrode based on the parent unsubstituted iron-tetraphenylporphyrin (**FeTPP**), the **UrFe** containing electrode exhibits a higher selectivity for CO_2-to-CO conversion with respect to H_2 production with at least one order of magnitude higher TOF and a marked stability. X-ray techniques support the molecular nature of the electrocatalytic events.

2. Experimental Section

2.1 Materials

Sodium dicarbonate ($NaHCO_3$) was purchased from Carlo Erba. N,N-Dimethylformamide (DMF), tetrabutylammonium hexafluorophosphate ($NBu4PF_6$), potassium chloride(KCl), perchloric acid ($HClO_4$) and multi-wall carbon nanotube (MWCNTs, 6-9 nm diameter 5 µm length, >95% Carbon) were obtained from Sigma-Aldrich. Toray carbon paper (TGP-H-60) was purchased from Alfa Aesar. All the chemicals were used as received without further purification. FeTPP was purchased from PorphyChem. Water was Milli-Q filtered (18.2 MΩ•cm at 25 °C). The synthesis of **UrFe** was prepared following the previously reported procedures. [27]

2.2 Apparatus

The UV-vis spectra of all materials were obtained between 490 nm to 1000 nm on a Varian Carry 5000 spectrophotometer. X-X-ray photoelectron spectroscopy (XPS) measurements were performed on a K Alpha spectrometer from Thermo Fisher, equipped with a monochromated X-ray Source (Al Kα, 1486.6 eV) with a spot size of 400 µm. The hemispherical analyzer was operated in CAE (Constant Analyzer Energy) mode, with a pass energy of 200 eV and a step of 1 eV for the acquisition of surveys spectra, and a pass energy of 50 eV and 20eV and a step of 0.1 eV for the acquisition of narrow spectra. A "dual beam" flood gun was used to neutralize the charge build-up. The spectra obtained were treated by means of the Avantage software, provided by Thermo Fisher. A Shirley type background subtraction was used and the peaks were analyzed using mixed Gaussian-Lorentzian curves (70% of Gaussian character). C1s spectra were further treated in order to eliminate the contribution of carbon paper substrate. Binding energies were calibrated against the sp2 C binding energy set a 284.5 eV. Transmission electron microscopy (TEM) images were obtained from Jeol 2100 Plus operating at 200 kV. Attenuated total reflectance Fourier-transform infrared (ATR-FTIR) spectra were recorded on a FT-IR Perkin Spectrum Two spectrometer. The dry **UrFe** film on the surface of ATR diamond accessory was obtained by drop-casting the dissolved **UrFe** molecule (before and after electrolysis) into dichloromethane and air dried for 10 minutes. Fe K-edge X-ray absorption near edge structure (XANES) data were collected on the LUCIA beamline [REF] of the Synchrotron SOLEIL at an electron energy of 2.7 GeV and a ring current of 500 mA. The incident photons energy was monochromatized y measn of a Si(111) double crystal monochromator and the data were collected as fluorescence excitation spectra with a Bruker SDD detector. The samples were placed in the experimental chamber under vacuum, with a 20° outgoing angle with respect to the detector. Fluorescence data were normalized to the intensity of the incoming beam and reduced using the Athena software.

2.3 Preparation of CNT-Ur and CNT-FeTPP

UrFe (6.4 mg, 3.5×10^{-3} M) and 6.4 mg MWCNTs were separately dissolved in 1 mL DMF and sonicated for 30 minutes then the the two suspension solutions were mixed together and sonicated for another 30 minutes and stirred overnight. The as prepared ink was immediately used or can be stored in the fridge and be used for a few days. The modified electrode was prepared by drop-casting the ink onto the surface of glassy carbon electrodes (GCEs, for CVs) or carbon paper (CP, size 10mm*10mm, for bulk electrolysis), and drying it in fume hood overnight to form a homogeneous film. Catalyst concentration on GCEs or CP was found to be 52 nmol cm^2. Electrodes with **CNT-FeTPP** was obtained using the same method.

2.4 Electrochemical characterization

All electrochemical experiments were performed on a Metrohm Autolab 302N potentiostat. Homogeneous cyclic voltammograms of **UrFe** were performed in a three-electrode electrochemical cell, composed of a GCE working electrode, SCE reference electrode and a platinum wire counter electrode. NBu_4PF_6 in DMF was utilized as the electrolyte.

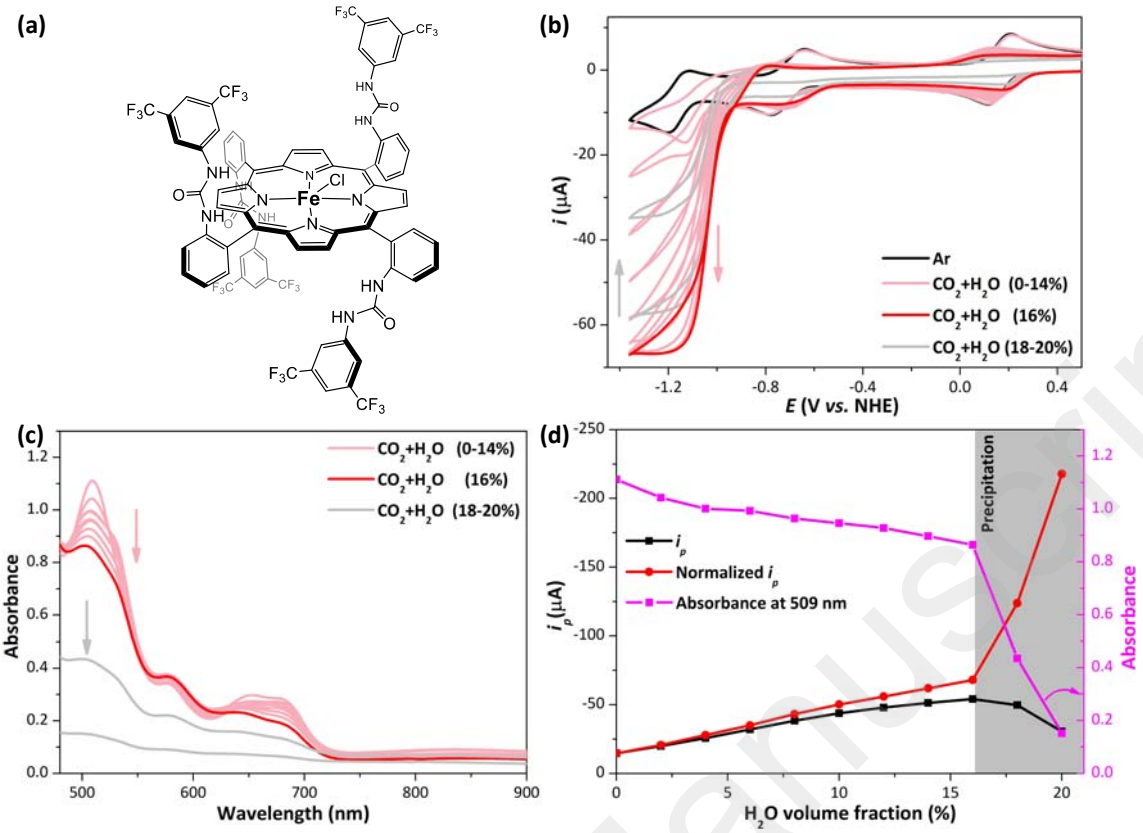

Figure 1 (a) Chemical structure of **UrFe**. (b) CVs of 1 mM **UrFe** in DMF containing 0.1 M NBu_4PF_6 under Ar (black), under CO_2 with 0-14% H_2O (light red curve), 16% H_2O (red) and 18-20% H_2O (light grey) at scan rate of 0.1 V s^{-1}. (c) UV-vis of 1 mM **UrFe** in DMF containing 0.1 M NBu_4PF_6 under CO_2 with 0-14% H_2O (light red), 16% H_2O (red) and 18-20% H_2O (light grey). (d) i_p (black), normalized i_p (red) and absorbance intensities (Q band of **UrFe** at 509 nm from UV-vis, magenta) under CO_2 against H_2O percent in electrolyte. The amount of soluble **UrFe** in electrolyte obtained from UV-vis was utilized to calculate the normalized i_p. The grey background is to show at which point **UrFe** precipitates due to the excess H_2O.

For heterogeneous catalysis, all controlled potential electrolysis and cyclic voltammetry experiments were conducted in a home-made H-cell with a modified GCEs or carbon paper working electrode, a saturated calomel reference electrode (SCE) and a platinum grill counter electrode with large surface area. $NaHCO_3$ in mQ water was used as the supporting electrolyte.

Potentials were converted to the normal hydrogen electrode (NHE) or reversible hydrogen electrode (RHE) for CVs or bulk electrolysis reference scale using the following formula:

$$E\ (\mathrm{V}\ vs.\ \mathrm{NHE}) = \text{Applied potential}\ (\mathrm{V}\ vs.\mathrm{SCE}) + 0.244\ \mathrm{V}$$
$$E(\mathrm{V}\ vs.\mathrm{RHE}) = \text{Applied potential}\ (\mathrm{V}\ vs.\mathrm{SCE}) + 0.244\ \mathrm{V} + 0.059\ \mathrm{V} \times \mathrm{pH}$$

2.5 Gas product analysis

Gas product analysis was performed with Micro Gas Chromatography (Micro-GC) from Chemlys company. The chromatographer is composed of two parallel modules, module A is a plot column with molecular sieve 10 m length, module B is a RT-Q-bond column of 12 m length. A Thermal Conductivity Detector (TCD) is used to identify and quantify gas products. The instrument allows automatized sampling and it was calibrated for CO_2, CO and H_2. The faradic efficiency of all experiments was determined using Micro-GC analysis results in the following equation, where Q is the charge consumed in bulk electrolysis, n is the number of electrons for CO or H_2 and F is the Faradic constant:

$$Faradic\ Efficiency\ (\%) = \frac{Q_{Experimental}}{Q_{Theoretical}} \times 100\% = \frac{n \times mol\ (CO\ or\ H_2) \times F}{Q} \times 100\%$$

3. Results and discussion

3.1 Effect of water in homogenous catalysis

In homogeneous catalysis, we have previously reported that the urea functions in the second coordination sphere of **UrFe** catalyst provide a multipoint hydrogen bonding scheme to bind and activate CO_2 for its reduction to CO which results in a remarkable drop in the overpotential of the catalytic reaction while conserving a high turnover frequency.[33] Interestingly, water was found to be a better proton source in CO_2-saturated DMF in comparison with more acidic trifluoroethanol and phenol proton sources commonly used to accelerate CO_2 electroreduction. Indeed, entrapped water molecules within the molecular clefts of **UrFe** were found to be responsible for routing the protons toward the metal active centre for the CO_2 reduction. We also determined that the protonation process was the rate limiting step of the catalysis. Thus, in order to

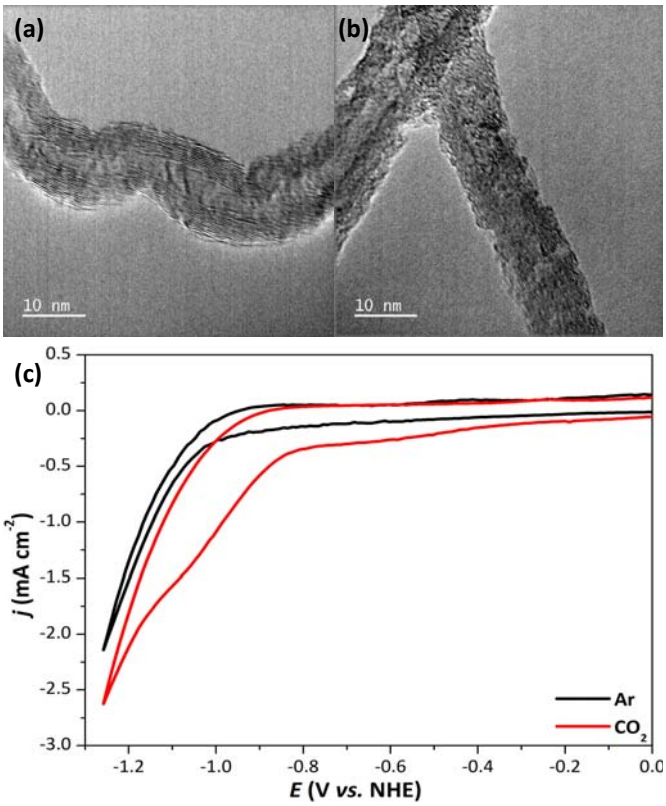

Figure 2 TEM images of (a) non-modified MWCNTs, (b) **UrFe** impregnated MWCNTs (**CNT-UrFe**). (c) CVs of **CNT-UrFe** drop casted on a 3mm diameter glassy carbon electrode under Ar (black) or CO_2-saturated (red, pH 6.73) 0.1 M $NaHCO_3$ aqueous solution at 0.1 V s^{-1} scan rate.

increase the rate of the reaction, we then thought of increasing the water content in DMF. Indeed, as shown in the cyclic voltammograms (CVs) of Figure 1b, the current intensity at the third reduction wave corresponding to formal redox couple $Fe^{0/I}$ (the first and second waves correspond respectively to the formal redox couples $Fe^{II/III}$ and $Fe^{I/II}$) CO_2 electroreduction increase with increasing water proportion in CO_2-saturated DMF. However, a maximum current intensity is reached at around 16% water in DMF before the current intensity starts decreasing (Figure 1c and 1d).

UV-vis analysis of the reaction media at different water proportions in DMF revealed that a severe drop in the intensity of the catalyst absorption bands also occurs at around 16% water content (Figure 1c and 1d). This decrease was attributed to the precipitation of the catalyst due to its hydrophobic character. The normalization of the current intensity by the amount of soluble catalyst determined by UV-vis shows that the beneficial effect of water on the reaction rate is clearly limited by the intrinsic hydrophobicity of the catalyst (Figure 1d). Interestingly, the transition at around 16% water content that causes the precipitation of the catalyst also enhances the catalytic performances of the remaining soluble catalyst. This transition probably corresponds to the solvents' reorganisation at the surface of the electrode when water goes from solute to solvent as reported for other binary solvent mixtures.[62] Using a DMF- and water-soluble catalyst, we have previously reported a similar catalytic enhancement when switching from DMF to water as a solvent for CO_2 electroreduction.[21]

Two options can be considered to overcome the limitation cause by the catalyst hydrophobicity, the first would consist of improving the its solubility in water by introducing hydrophilic groups on the porphyrin rim such as ionic groups of polyethylene glycol (PEG) chains. However, in addition to the long tedious synthetic route to introduce these extra functions on the catalyst, their presence on the periphery of the porphyrin can induce significant changes in the electronic structure of the catalyst and may also interfere with the second sphere interactions which would modify the initial reactivity observed for the catalyst. The second option, examined in this study, is the immobilization of the catalyst on the interface of a working electrode as part of a heterogenous electrochemical cell using water as a solvent and proton source. In addition to its fast and practical implementation compared to a catalyst modification approach, the heterogenization of the molecular catalyst also opens the way for reaction scaleup and device development for potential practical applications.

3.2 Modified electrode preparation and characterization

The ink employed in this study to modify the carbon paper electrode was prepared following the typical method that consist in sonicating a mixture containing the iron porphyrin catalyst (**UrFe**), MWCNTs in DMF.[63] The loss of the porphyrin's red color during the process is a clear indication of a successful MWCNTs impregnation with the catalyst. The change in morphology from the smooth walled MWCNTs to wrinkled walls (Figure 2a and 2b), as observed by Transmission Electron Microscopy (TEM), confirms the incorporation of the catalyst on the MWCNTs.

Prior to preparing the modified carbon paper electrode, the ink was drop-casted on a 3 mm diameter glassy carbon electrode for a first electrochemical evaluation. CV of the **CNT-UrFe** catalyst in 0.1 M $NaHCO_3$ aqueous solution under a CO_2 atmosphere shows a significant increase in the reductive current at a potential more negative than -0.4 V *vs.* NHE compared to that recorded under Ar (Figure 2c). This current becomes more and more prominent when sweeping to more negative potentials. Gas products analysis using gas chromatography (GC) during controlled potential electrolysis at -0.88 V *vs.* RHE for 30 min revealed that CO is the major product with a faradic efficiency higher than 78% (Figure S1). Nuclear magnetic resonance (NMR) analysis of the electrolyte excluded the formation of liquid products such as format, formaldehyde or methanol during the electrolysis.

In order to increase the surface as well as the specific surface of the electrode, the **CNT-UrFe** ink was then drop-casted on the surface of a 10x10 mm carbon paper electrode and the catalytic performances of the obtained modified electrode were evaluated in controlled potential electrolysis for CO_2 reduction at -0.48, -0.58, -0.68, 0.78, -0.88 and -0.98 V *vs.* RHE for 120 min. A stable current density was observed from -0.48 to -0.88 V during the total duration of the electrolysis (Figure 3). At

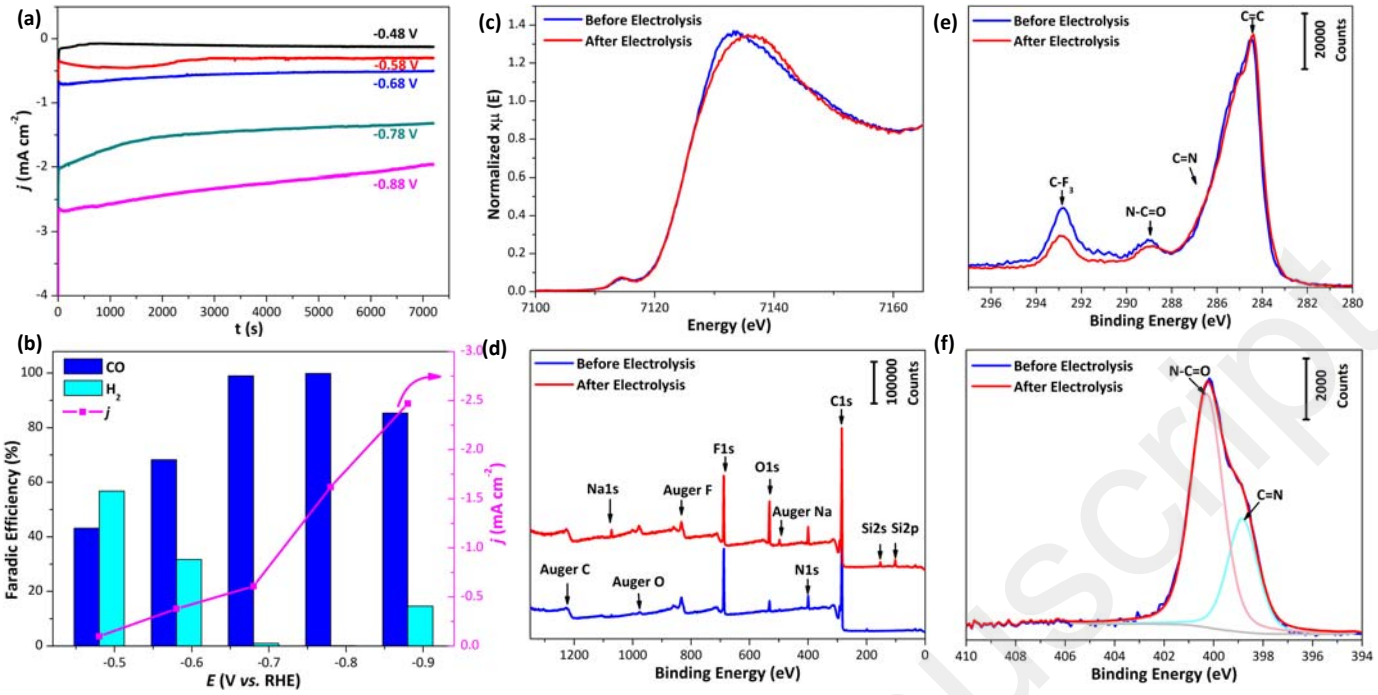

Figure 3 (a) Current density vs. time of controlled potential electrolysis of **CNT-UrFe**/CP in CO_2-saturated 0.1 M $NaHCO_3$ aqueous solutions. (b) Faradic efficacy of CO (blue column) and H_2 (cyan column) and average current density (magenta curve) at different potentials after 1 hour electrolysis. (c) Fe K-edge XANES spectra of **CNT-UrFe**/CP before (blue) and after electrolysis (red). (d) XPS survey of **CNT-UrFe**/CP before (blue) and after electrolysis (red). (e) XPS spectra for the C1s region of **CNT-UrFe**/CP before (blue) and after electrolysis (red). (f) XPS spectra for N1s region of **CNT-UrFe**/CP before (blue), after electrolysis (red) and deconvolution of N-C=O (light red) and C=N (cyan).

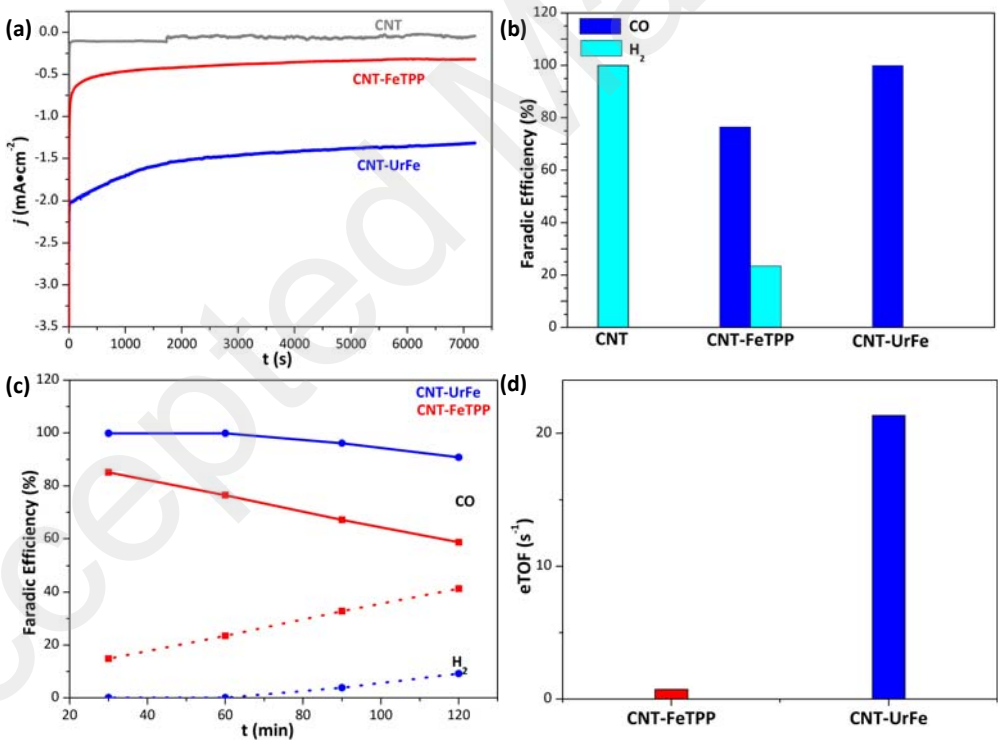

Figure 4 Controlled potential electrolysis of non-modified **CNT** (gray), **CNT-FeTPP** (red) and **CNT-UrFe** (blue) on carbon paper in CO_2-saturated 0.1 M $NaHCO_3$ aqueous solutions at -0.78 V vs. NHE. (b) Faradic efficiency of CO (blue column) and H_2 (cyan column) after 1 hour electrolysis, (c) Faradic efficiency of CO for CNT-FeTPP/CP (solid red) and **CNT--UrFe**/CP (solid blue) and Faradic efficiency of H_2 for **CNT-FeTPP**/CP (dash red) and **CNT--UrFe**/CP (dash blue) during 2 hours electrolysis, (d) eTOF of **CNT-FeTPP** and **CNT-UrFe** after 1 hour electrolysis.

potentials more negative than -0.88 V, the current density becomes less stable, probably due to the alteration of the catalyst at the surface of the electrode (Figure S2). Results from GC monitoring of the gas products for 60 min indicate that the highest selectivity for CO production (99.9%) was reached at –0.78 V (Figure 3b, Table S1). The loss of stability and/or selectivity that pop up at potentials higher than - 0.78 V, lead us to lock further investigation at -0.78 V.

Table 1 Comparison of catalytic activity of **CNT-UrFe** with other immobilized catalysts for CO_2 reduction.

#	Catalysts (Electrolysis V vs. RHE, pH)	Active Fe center $\times 10^{-9} mol/cm^2$	j mA cm^{-2}	FE CO/H_2 %	eTOF s^{-1}	Reference
1	**CNT-UrFe** (-0.78V, pH 6.7)	0.4	1.62	99.9 / 1.5	21.3	This work
2	**CNT-UrFe** (-0.88V, pH 6.7)	0.4	2.47	85.4 / 9.2	27.3	This work
3	**CNT-FeTPP** (-0.78V, pH 6.7)	2.5	0.45	76.5 / 25.0	0.7	This work
4	CoFPc (-0.79V, pH 7.2)	13	4.5	93 / 5	1.6	32
5	COF-367-Co (-0.65V, pH 7.3)	2	0.45	53 / 62	0.62	58
6	CAT_{pyr}/MWCNT (-0.59V, pH 7.3)	24	0.2	93 / 4	0.04	54
7	CAT_{CO2H}/MWCNT (-0.62V, pH 7.3)	6.4	0.16	80 / n.a.	0.1	44
8	CoTPP/SWCNT (-0.68V, pH 7.2)	170	3.2	85 / 9	0.08	59
9	FeTPP/SWCNT (-0.68V, pH 7.2)	170	0.9	64 / 9	0.08	59
10	CMK-FeTPP (-0.89V, pH4.2)	0.9	1.16	90.7 / 10.2	6.2	64
11	CoPc-A/Graphene (-0.70V, pH 6.8)	3.1	5.0	74 / 27	6	65
12	Fe-PB/MWCNT (-0.63V, pH 7.3)	3.7	0.49	100 / 0	1.5	61
13	Fe-PB/MWCNT (-0.78V, pH 7.3)	3.7	1.5	95 / 5	4.5	61
14	FeTPP/MWCNT (-0.63V, pH 7.3)	2.5	0.22	96 / 6	1.0	61
15	FeTPP/MWCNT (-0.78V, pH 7.3)	2.5	0.6	78 / 22	2.5	61
16	CoPPc/CNT (-0.51V, pH7.4)	440	12	80-90 / n.a.	0.2	66
17	CoPc/MWCNT (-0.47V, pH 6.8)	18	1.4	59 / n.a.	0.2	67
18	CoPc/MWCNT (-0.64V, pH 6.8)	18	10.0	92 / 6	2.7	67
19	CoPc/MWCNT (-0.62V, pH 7.2)	18	15.0	98 / 3	4.1	67
20	FePGF (-0.59V. pH 4.2)	1.3	0.2	97.0 / 4.0	0.8	68
21	D-P-CoPc/Ketjen black (-0.61V, pH 7.3)	111	2.5	97 / n.a.	0.1	69

n. a. represents not available

Accordingly, we first interrogated the stability of the catalyst during the electrolysis at -0.78 V. X-ray photoelectron spectroscopy (XPS) spectra performed on the **CNT-UrFe**/CP electrode before and after electrolysis showed similar peaks for C1s, N1s and F1s with extra peaks appearing after electrolysis and corresponding to Na1s and O1s coming respectively from water and $NaHCO_3$ in the electrolyte and Si2s and Si2p coming from sintered glass in the filters of the electrochemical cell (Figure 3d). Notably, N1s and C1s high resolution spectra before and after electrolysis show also similar N-C=O (Urea), C=N and C-F contributions (Figure 3e and 3f) indicating that the electrolysis does not induce a major change in the catalyst structure. Unfortunately, because of the strong F1s-loss signal (24 fluorine atoms per catalyst molecule) the Fe1s peak cannot be observed. XPS being a surface technique, we also gathered evidences on the structure of our catalyst using the bulk-sensitive X-ray absorption spectroscopy. We collected the Fe K-edge XANES spectra on **CNT-UrFe** modified electrode before and after 2 hours electrolysis (Figure 3c). In both cases, pre- and rising-edge have identical energy positions with only minor spectral changes due probably to the exchange of the chloride by a hydroxide axial ligand during the electrolysis. XANES

spectrum of the modified electrode after 2 hours electrolysis was also compared to that of an Fe_2O_3 modified electrode as well as metallic iron to exclude the formation of iron nanoparticles as a result of the catalyst degradation (Figure S4). No corresponding signatures to either Fe_2O_3 or metallic iron were evidenced ruling out the presence of such species and ascertain the molecular nature of the catalytic species. The stability of the catalyst was also confirmed by Fourier-transform infrared spectroscopy (FTIR) analysis corroborating that the catalyst does not undergo significant structural changes during the electrolysis (Figure S5).

3.3 Second sphere effect in heterogenous catalysis

In homogeneous CO_2-to-CO electrocatalytic reduction, the urea groups in **UrFe** were shown to induce multipoint hydrogen-bonding interactions with the substrate that lead to a better capture and a remarkable improvement of the catalytic performances. To examine if similar second coordination sphere effects are operating also under heterogenous catalysis, the catalytic properties of the **CNT-UrFe** modified electrode were systematically compared to those of a similar electrode embarking **CNT-FeTPP**. Under similar controlled potential electrolysis experiments, the **UrFe** containing electrode exhibits four times higher current density than that of the electrode based on **CNT-FeTPP** (Figure 4a). Nevertheless, **CNT-FeTPP** still displays a significantly higher current density than that when only MWCNTs are present on the surface of the electrode. Therefore, GC analysis of gas products after a 2 hours electrolysis revealed that CO is produced above 90% FE selectivity in the case of **UrFe** and nearing a low 60% FE for the **FeTPP**. In order to calculate the effective turnover frequency (eTOF) of the **CNT-UrFe** modified electrode,[65] the amount of electrochemically active catalyst on the surface of the electrode was determined to be 0.4 nmol cm^{-2} by integrating the peak of the $Fe^{III/II}$ redox couple, then matching this value with the amount of CO produced (Figure S6) gives an eTOF of 21 s^{-1} for **UrFe** containing electrode, a value 20 times higher than that of a **FeTPP**-containing electrode (0.9 s^{-1}). To the best of our knowledge, such a catalytic activity places the **UrFe** as the highest reported eTOF value in the literature (Table 1). Thus, our results clearly outline the important impact of added functionalities such as hydrogen bonding donor groups to enhance the electrocatalytic activity from homogeneous to heterogeneous catalysis. Furthermore, the selectivity for CO_2-to-CO process was also privileged to the side production of H_2. **UrFe** displays also a better long-term stability than that of a **FeTPP**. Indeed, although the current density stays stable in both cases for 2 hours, the reaction selectivity for CO production drops from 85% at 30 min to less than 58% after 2 hours in the case of **FeTPP** whereas over 90% selectivity is maintained for **UrFe** during the total time of the experiment (Figure 4c).

Conclusions

Cost-effective catalysts and catalytic technologies for the conversion of CO_2 to energy rich content molecules are the hard challenges for chemists to surmount in order to road us towards sustainability. Important advancement in design of molecular catalysts containing three dimensional facets as prevail at active sites of enzymes, have boosted their electrocatalytic power. Bringing molecular catalysts with this added dimensionality on the surface of electrodes can indeed help to reach better performances on different grounds such as selectivity, reaction rates and stability. We have shown in this report that the presence of added dimensionality of urea groups that function as molecular clefts towards the binding of CO_2 and developing network of hydrogen bonding with water molecules for conveying protons in homogeneous catalysis can also be transferred in a heterogeneous stance that resulted in the highest eTOF of molecular catalyst at the surface of carbonaceous electrode. The selective electrochemical performance towards CO production in comparison with the naked parent porphyrin derivative is also a salient feature. Furthermore, the gain in stability of the modified electrodes upon electrocatalytic runs can be inferred to a better management of the active CO_2 form prevent intramolecular alterations as recently reported.[70]

Our results therefore point to the remarkable gain when bringing added functionalities on molecular catalysts at the surface of electrodes. We are currently pursuing our effort in bringing the best bits from the design of homogeneous catalysts for the fabrication of a device for the (photo)electrochemical CO_2 conversion.

Author Contributions

We acknowledge the following author contributions based onCRediT classification: Zakaria Halime and Ally Aukauloo: Conceptualization, Funding acquisition, Supervision and Writing – original draft. Chanjuan Zhang, Diana Dragoe, François Brisset, Bernad Boitrel, Benedikt Lassalle-Kaiser and Winfried Leibl: Investigation and Writing – review & editing. All authors have read and agreed to the published version of the manuscript.

Conflicts of interest

There are no conflicts to declare.

Acknowledgements

This work has been supported by the French National Research Agency (LOCO, grant N°: ANR-19-CE05-0020-02 and Labex charmmmat, grant N°: ANR-11-LABX-0039). We thank CNRS, CEA Saclay, ICMMO and University Paris-Saclay for the financial support. We thank the China Scholarship Council for supporting C. Zhang (CSC student number 201904910525). We also thank the analytical support facility at ICMMO for their help with XPS and TEM analysis.

Notes and references

1. J. H. Montoya, L. C. Seitz, P. Chakthranont, A. Vojvodic, T. F. Jaramillo and J. K. Norskov, *Nat Mater*, 2016, **16**, 70-81.
2. P. B. Pati, R. Wang, E. Boutin, S. Diring, S. Jobic, N. Barreau, F. Odobel and M. Robert, *Nat Commun*, 2020, **11**, 3499.
3. S. C. Roy, O. K. Varghese, M. Paulose and C. A. Grimes, *ACS Nano*, 2010, **4**, 1259-1278.
4. E. E. Benson, C. P. Kubiak, A. J. Sathrum and J. M. Smieja, *Chem. Soc. Rev.*, 2009, **38**, 89-99.
5. L. Zhang, Z.-J. Zhao and J. Gong, *Angew. Chem. Int. Ed.*, 2017, **56**, 11326-11353.
6. C. Costentin, S. Drouet, M. Robert and J.-M. Savéant, *Science*, 2012, **338**, 90-94.
7. C. Costentin, M. Robert and J.-M. Savéant, *Acc. Chem. Res.*, 2015, **48**, 2996-3006.
8. J.-H. Jeoung and H. Dobbek, *Science*, 2007, **318**, 1461-1464.
9. M. Can, F. A. Armstrong and S. W. Ragsdale, *Chem. Rev.*, 2014, **114**, 4149-4174.
10. A. M. Appel, J. E. Bercaw, A. B. Bocarsly, H. Dobbek, D. L. DuBois, M. Dupuis, J. G. Ferry, E. Fujita, R. Hille, P. J. A. Kenis, C. A. Kerfeld, R. H. Morris, C. H. F. Peden, A. R. Portis, S. W. Ragsdale, T. B. Rauchfuss, J. N. H. Reek, L. C. Seefeldt, R. K. Thauer and G. L. Waldrop, *Chem. Rev.*, 2013, **113**, 6621-6658.
11. C. Costentin and J.-M. Savéant, *Nat. Rev. Chem.*, 2017, **1**, 0087.
12. A. W. Nichols and C. W. Machan, *Front. Chem.*, 2019, **7**.
13. Y. Matsubara, *Acs Energy Lett*, 2019, **4**, 1999-2004.
14. P. Gotico, Z. Halime and A. Aukauloo, *Dalton Trans.*, 2020, **49**, 2381-2396.
15. C. Costentin, M. Robert, J.-M. Savéant and A. Tatin, *Proc. Natl. Acad. Sci. USA*, 2015, **112**, 6882-6886.
16. C. G. Margarit, C. Schnedermann, N. G. Asimow and D. G. Nocera, *Organometallics*, 2019, **38**, 1219-1223.
17. K. Guo, X. L. Li, H. T. Lei, W. Zhang and R. Cao, *Chemcatchem*, 2020, **12**, 1591-1595.
18. S. Sinha and J. J. Warren, *Inorg. Chem.*, 2018, **57**, 12650-12656.
19. C. G. Margarit, N. G. Asimow, M. I. Gonzalez and D. G. Nocera, *The Journal of Physical Chemistry Letters*, 2020, **11**, 1890-1895.
20. I. Azcarate, C. Costentin, M. Robert and J.-M. Savéant, *J. Am. Chem. Soc.*, 2016, **138**, 16639-16644.
21. A. Khadhraoui, P. Gotico, B. Boitrel, W. Leibl, Z. Halime and A. Aukauloo, *Chem. Commun.*, 2018, **54**, 11630-11633.
22. A. Khadhraoui, P. Gotico, W. Leibl, Z. Halime and A. Aukauloo, *ChemSusChem*, 2021, **14**, 1308-1315.
23. P. Sen, B. Mondal, D. Saha, A. Rana and A. Dey, *Dalton Trans*, 2019, **48**, 5965-5977.
24. E. Nichols, J. S. Derrick, S. K. Nistanaki, P. T. Smith and C. J. Chang, *Chem. Sci.*, 2018, **9**, 2952-2960.
25. C. K. Williams, A. Lashgari, J. A. Tomb, J. Chai and J. J. Jiang, *Chemcatchem*, 2020, **12**, 4886-4892.
26. Y. Yang and F. Li, *Current Opinion in Green and Sustainable Chemistry*, 2021, **27**, 100419.
27. S. Sato, B. J. McNicholas and R. H. Grubbs, *Chem. Commun.*, 2020, DOI: 10.1039/D0CC00791A.
28. A. Tatin, C. Comminges, B. Kokoh, C. Costentin, M. Robert and J. M. Saveant, *Proc Natl Acad Sci U S A*, 2016, **113**, 5526-5529.
29. S. Kreft, R. Schoch, J. Schneidewind, J. Rabeah, E. V. Kondratenko, V. A. Kondratenko, H. Junge, M. Bauer, S. Wohlrab and M. Beller, *Chem*, 2019, **5**, 1818-1833.
30. M. Schreier, L. Curvat, F. Giordano, L. Steier, A. Abate, S. M. Zakeeruddin, J. Luo, M. T. Mayer and M. Gratzel, *Nat Commun*, 2015, **6**, 7326.
31. H. Park, H.-H. Ou, A. J. Colussi and M. R. Hoffmann, *The Journal of Physical Chemistry A*, 2015, **119**, 4658-4666.
32. N. Morlanés, K. Takanabe and V. Rodionov, *ACS Catalysis*, 2016, **6**, 3092-3095.
33. P. Gotico, B. Boitrel, R. Guillot, M. Sircoglou, A. Quaranta, Z. Halime, W. Leibl and A. Aukauloo, *Angew. Chem. Int. Ed.*, 2019, **58**, 4504-4509.
34. P. Gotico, L. Roupnel, R. Guillot, M. Sircoglou, W. Leibl, Z. Halime and A. Aukauloo, *Angew. Chem. Int. Ed. Engl.*, 2020, **59**, 22451-22455.
35. E. Boutin, L. Merakeb, B. Ma, B. Boudy, M. Wang, J. Bonin, E. Anxolabehere-Mallart and M. Robert, *Chem. Soc. Rev.*, 2020, **49**, 5772-5809.
36. F. Franco, C. Rettenmaier, H. S. Jeon and B. Roldan Cuenya, *Chem. Soc. Rev.*, 2020, **49**, 6884-6946.
37. K. E. Dalle, J. Warnan, J. J. Leung, B. Reuillard, I. S. Karmel and E. Reisner, *Chem Rev*, 2019, **119**, 2752-2875.
38. N. Corbin, J. Zeng, K. Williams and K. Manthiram, *Nano Research*, 2019, **12**, 2093-2125.
39. S. A. Yao, R. E. Ruther, L. Zhang, R. A. Franking, R. J. Hamers and J. F. Berry, *J. Am. Chem. Soc.*, 2012, **134**, 15632-15635.
40. C. C. L. McCrory, A. Devadoss, X. Ottenwaelder, R. D. Lowe, T. D. P. Stack and C. E. D. Chidsey, *J. Am. Chem. Soc.*, 2011, **133**, 3696-3699.
41. M. V. Sheridan, K. Lam and W. E. Geiger, *J. Am. Chem. Soc.*, 2013, **135**, 2939-2942.
42. A. Zhanaidarova, C. E. Moore, M. Gembicky and C. P. Kubiak, *Chem. Commun.*, 2018, **54**, 4116-4119.
43. T. Atoguchi, A. Aramata, A. Kazusaka and M. Enyo, *J. Chem. Soc., Chem. Commun.*, 1991, DOI: DOI 10.1039/c39910000156, 156-157.
44. A. Maurin and M. Robert, *Chem. Commun.*, 2016, **52**, 12084-12087.
45. E. A. Mohamed, Z. N. Zahran and Y. Naruta, *Chem. Mater.*, 2017, **29**, 7140-7150.
46. M. Zhu, J. Chen, L. Huang, R. Ye, J. Xu and Y.-F. Han, *Angew. Chem. Int. Ed.*, 2019, **58**, 6595-6599.
47. C. R. Cabrera and H. D. Abruña, *J. Electroanal. Chem. Interf. Electrochem.*, 1986, **209**, 101-107.
48. T. R. O'Toole, B. P. Sullivan, M. R. M. Bruce, L. D. Margerum, R. W. Murray and T. J. Meyer, *J. Electroanal. Chem. Interf. Electrochem.*, 1989, **259**, 217-239.
49. D. Quezada, J. Honores, M. J. Aguirre and M. Isaacs, *J. Coord. Chem.*, 2014, **67**, 4090-4100.
50. D. Quezada, J. Honores, M. García, F. Armijo and M. Isaacs, *New J. Chem.*, 2014, **38**, 3606-3612.
51. J. A. Mann, J. Rodríguez-López, H. D. Abruña and W. R. Dichtel, *J. Am. Chem. Soc.*, 2011, **133**, 17614-17617.
52. J. D. Blakemore, A. Gupta, J. J. Warren, B. S. Brunschwig and H. B. Gray, *J. Am. Chem. Soc.*, 2013, **135**, 18288-18291.
53. Y. Okabe, S. K. Lee, M. Kondo and S. Masaoka, *J. Biol. Inorg. Chem.*, 2017, **22**, 713-725.
54. A. Maurin and M. Robert, *J. Am. Chem. Soc.*, 2016, **138**, 2492-2495.
55. N. Sonoyama, M. Kirii and T. Sakata, *Electrochem. Commun.*, 1999, **1**, 213-216.
56. J. Shen, R. Kortlever, R. Kas, Y. Y. Birdja, O. Diaz-Morales, Y. Kwon, I. Ledezma-Yanez, K. J. P. Schouten, G. Mul and M. T. M. Koper, *Nat. Commun.*, 2015, **6**, 8177.
57. Z. Weng, J. Jiang, Y. Wu, Z. Wu, X. Guo, K. L. Materna, W. Liu, V. S. Batista, G. W. Brudvig and H. Wang, *J. Am. Chem. Soc.*, 2016, **138**, 8076-8079.

58. S. Lin, C. S. Diercks, Y.-B. Zhang, N. Kornienko, E. M. Nichols, Y. Zhao, A. R. Paris, D. Kim, P. Yang, O. M. Yaghi and C. J. Chang, *Science*, 2015, **349**, 1208-1213.
59. X.-M. Hu, M. H. Rønne, S. U. Pedersen, T. Skrydstrup and K. Daasbjerg, *Angew. Chem. Int. Ed.*, 2017, **56**, 6468-6472.
60. S. Aoi, K. Mase, K. Ohkubo and S. Fukuzumi, *Chem. Commun.*, 2015, **51**, 10226-10228.
61. P. T. Smith, B. P. Benke, Z. Cao, Y. Kim, E. M. Nichols, K. Kim and C. J. Chang, *Angew. Chem. Int. Ed.*, 2018, **57**, 9684-9688.
62. A. M. Buchbinder, E. Weitz and F. M. Geiger, *J. Am. Chem. Soc.*, 2010, **132**, 14661-14668.
63. M. Abdinejad, C. Dao, B. Deng, M. E. Sweeney, F. Dielmann, X.-a. Zhang and H. B. Kraatz, *ChemistrySelect*, 2020, **5**, 979-984.
64. J. Choi, J. Kim, P. Wagner, J. Na, G. G. Wallace, D. L. Officer and Y. Yamauchi, *J Mater Chem A*, 2020, **8**, 14966-14974.
65. J. Choi, P. Wagner, S. Gambhir, R. Jalili, D. R. MacFarlane, G. G. Wallace and D. L. Officer, *ACS Energy Letters*, 2019, **4**, 666-672.
66. N. Han, Y. Wang, L. Ma, J. Wen, J. Li, H. Zheng, K. Nie, X. Wang, F. Zhao, Y. Li, J. Fan, J. Zhong, T. Wu, D. J. Miller, J. Lu, S.-T. Lee and Y. Li, *Chem*, 2017, **3**, 652-664.
67. X. Zhang, Z. Wu, X. Zhang, L. Li, Y. Li, H. Xu, X. Li, X. Yu, Z. Zhang, Y. Liang and H. Wang, *Nat Commun*, 2017, **8**, 14675.
68. J. Choi, P. Wagner, R. Jalili, J. Kim, D. R. MacFarlane, G. G. Wallace and D. L. Officer, *Advanced Energy Materials*, 2018, **8**, 1801280.
69. H. Wu, M. Zeng, X. Zhu, C. Tian, B. Mei, Y. Song, X.-L. Du, Z. Jiang, L. He, C. Xia and S. Dai, *ChemElectroChem*, 2018, **5**, 2717-2721.
70. A. N. Marianov, A. S. Kochubei, T. Roman, O. J. Conquest, C. Stampfl and Y. J. Jiang, *Acs Catalysis*, 2021, **11**, 3715-3729.